Physics implications of shape on biological function
Pomp, W.

Citation
Pomp, W. (2017, December 5). *Physics implications of shape on biological function. Casimir PhD Series*. Retrieved from https://hdl.handle.net/1887/57789

Cover Page

The handle http://hdl.handle.net/1887/57789 holds various files of this Leiden University dissertation

Author: Pomp, Wim
Title: Physics implications of shape on biological function
Date: 2017-12-05

Chapter 3

Control of membrane mechanics by light-induced lipid oxidation[†]

Biological systems exhibit a variety of different lipid mixes. Locally, patches of lipids can aggregate and form patches on the membrane which have distinct properties from the rest of the membrane. We investigated the change in membrane properties during the formation of these patches by employing a novel system employing light to induce phase separation in giant unilamellar vesicles. In this process spatial and temporal fluctuations in the membrane are apparent. We show that the speed of patch generation is dependent on the amount of light. Furthermore, we show that the membrane tension drops following a power law as can be expected from a phase transition. However, it does not exhibit universal behavior.

[†]This chapter is based on: W. Pomp, M. Rinaldin and T. Schmidt "Inducing phase separation in GUV's". *In preparation.*

3.1   Introduction

Oxidation of biomolecules, and in particular lipids, plays an important role in physiology and in health. Processes associated with aging [1, 2] are largely governed by the oxidation of molecules in the cell, there is clearly documented evidence for a strong correlation between oxidation and cancer progression [3–6], and it is known that excessive oxidation will lead to cell death [7]. These correlations have also been utilized in medical therapy. Spatially controlled oxidation is used in photodynamic therapy (PDT) [8] to treat e.g. tumors of the skin. In PDT tumor tissue is covered with light-sensitive molecules, which on excitation by light produce local reactive oxygen species that oxidize molecules in their surrounding, finally leading to cell death in the tumor tissue. The molecular origin of oxidation is related to various reactive oxygen species, among which singlet oxygen ($^1O_2$) is the most prominent. The processes that drive cell death by oxidative stress are very diverse and still not conclusively understood [9, 10]. Yet, it is believed that a change of the cell membrane by reactive oxygen species is one of the aspects that will lead to cell death [11].

The membrane of a cell is a two-dimensional fluid comprised of a bilayer of a vast mixture of lipids and proteins [12–14]. Lately, it has become clear that the function of proteins is strongly modulated by their lipid environment [15, 16]. This modulation can be of pure chemical nature due to a direct interaction of the protein with a lipid or be based on the physical and mechanical properties of the cell membrane. The latter effects are associated to the rich phase-state a lipid membrane can undergo. Although still fluid, characterized by the unrestricted mobility of components, lipid membranes can assume ordering in their tail region known as liquid-ordered and liquid-disordered, two states that have very different mechanical properties. The transition temperature between states strongly depends on the lipid type and in particular on any double bonds in the acyl chains of the lipid tail. Given that the cell membrane is composed of a large variety of different lipids it is not too surprising that fluid membranes of more components display even richer behavior, including phase-separated regions and phase-boundaries with spatially inhomogeneous physical and mechanical properties [17, 18], all modulating cell behavior [19]. Diffusion of proteins might be impaired by phase borders, or some patches of lipid might have a different curvature, controlling the binding of curvature sensing proteins [20], whose affinity depends on the local curvature of the membrane. Hence, the understanding of the influence of lipid oxidation on the physical and mechanical properties of mixed membranes is important for its implication in cells, health, and disease.

To investigate the change in physical and mechanical properties of mixed membranes on controlled oxidation we imaged giant unilamellar vesicles (GUVs). For controlled oxidation, we used a molecular system in which reactive oxygen species were generated by light [1, 2, 21]. Rhodamine-labeled lipids were introduced at low concentration into the membrane of GUVs. On excitation by light, the rhodamine fluorophores generated singlet oxygen in their direct vicinity. Singlet oxygen, in turn, reacted with lipid molecules leading to local oxidation and local change in lipid and membrane properties. The latter included the formation and growth of phase-separated regions, a change in membrane surface area, and a change in membrane tension. Change in these led to dramatic shape fluctuations, the properties of which we qualitatively describe here for the first time.

3.2 Results

3.2.1 Light-induced phase separation

We prepared giant unilamellar vesicles (GUVs) from a mixture of the lipids (1-palmitoyl-2-oleoyl-*sn*-glycero-3-phosphocholine (POPC), 1,2-dioleoyl-*sn*-glycero-3-phosphoethanolamine-N-(lissamine rhodamine B sulfonyl) (DOPE-rhodamine)), sphingomyelin (SM) together with cholesterol (Chol). The mixture was chosen such that it formed a homogeneous phase within the ternary phase diagram at room temperature (figure 3.1). A low amount (5%) of rhodamine-DOPE was added to allow for observation of the GUV membrane in a fluorescence microscope. At low-light observation conditions (561 nm, $100\,\mathrm{W/cm^2}$) the fluorescence was homogeneously distributed on the GUV membrane, the shape of which was spherical.

In order to induce reactive oxygen species, the excitation intensity was increased to $1.4\,\mathrm{kW/cm^2}$ at activation conditions. Excitation of the rhodamine dye, transferred the dye into its excited triplet-state at small probability (1-3%) which, in sequence, leads in part to a spin exchange with a nearby oxygen molecule, and the creation of a highly reactive singlet-oxygen species ($^1O_2$). The singlet-oxygen will react with high efficiency with nearby molecules, among which lipids that contain double-bonds in their aliphatic chains [21]. Such reaction will result in a shift of the lipid shape (figure 3.2) and melting temperature, essentially moving the lipid mixture in the ternary phase diagram of the GUV to the right into the unmixing region (see arrow in figure 3.1) .
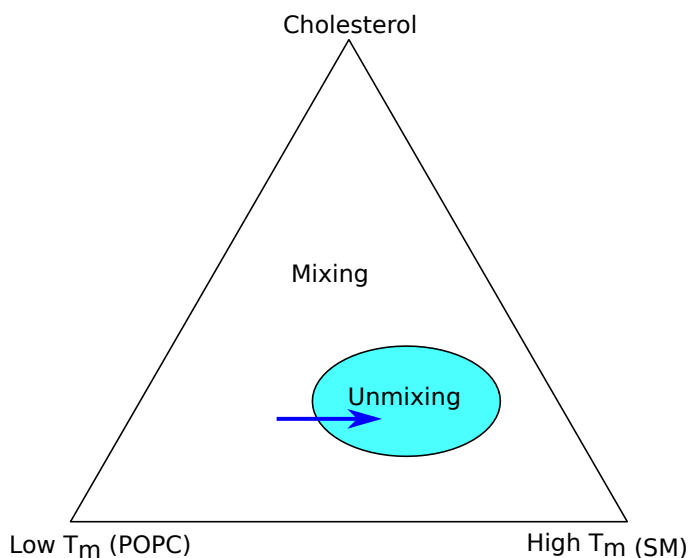
Figure 3.1: **Ternary phase diagram of a three lipid mixture.** Cholesterol and lipids of high (DOPC) and of low melting-temperature (DOPE) were mixed at a ratio that the initial composition was outside the unmixing region. On activation by light, lipids were oxidized and the mixture moved into the unmixing region.

We added a low amount ($\approx 1\%$) of rhodamine-conjugated lipids to visualize the GUV membrane in a wide-field fluorescence microscope (figure 3.3). It has been shown that rhodamine-DOPE preferentially resides in the liquid-ordered part of the membrane [17, 18], making it ideal for following phase separation to occur. We focused the microscope into the equatorial plane of the GUV. The depth-of-focus of our optical system was $\approx 1\,\mu\text{m}$, much smaller than the typical vesicle size of 20 to 50 µm. In this imaging setting, the GUV's perimeter was visible at high contrast. At the beginning of the experiment ($t = 0\,\text{s}$), the fluorescence was homogeneously distributed along the perimeter (figure 3.3 top-left), a signature of the lipid mixture to assume a single homogeneous phase. The small top-bottom gradient in fluorescence seen in figure 3.3 was due to an inhomogeneous illumination for the GUV shown. Where the fluorescence was homogeneous for the initial condition (figure 3.3 top-left) the distribution of the rhodamine-DOPE turned increasingly inhomogeneous during the experiment. This became most obvious after many (figure 3.3 bottom;
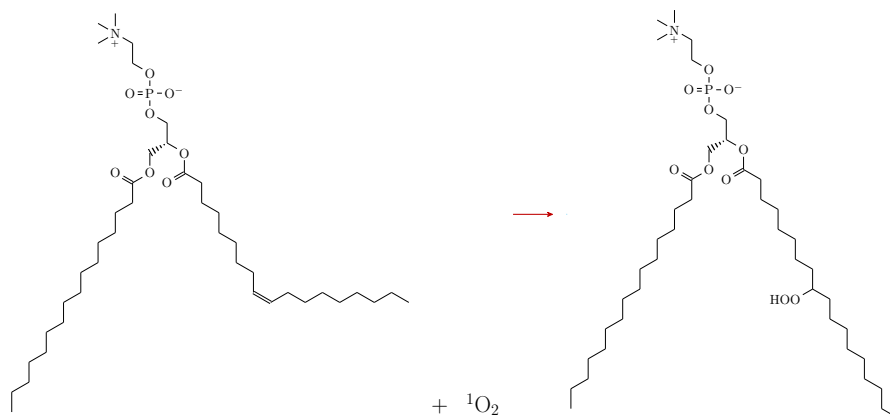
Figure 3.2: **Oxidation reaction in (1,2)-dioleoyl-*sn*-glycero-3-phosphocholine (DOPC).** Oxidation of the double-bond will lead to a change in the shape of DOPC and a larger surface area of the lipid [21].

$> 70\,s$) activation/observation cycles. Apparently, lipid oxidation drove the lipid system from the fully mixed into the unmixed region in figure 3.1, as has been reported previously [21]. Given that the rhodamine-DOPE preferentially partitions into the liquid-ordered phase [17, 18] the fluorescence on the GUV membrane became patchy.

3.2.2 Lipid oxidation and phase separation depends on fluorophore concentration and illumination intensity

The observed patchiness was further used to quantify the rate of photoconversion and for the characterization of its molecular origin. Phase separation into liquid-ordered and liquid-disordered membrane domains became visible when the fluorescent lipids started to be confined in liquid-ordered patches of a size larger than the diffraction limit ($\approx 300\,nm$). For quantification, we analyzed the fluorophore distribution along the perimeter of the GUV by means of the pixel brightness. This analysis allowed us to obtain the line profile which, when phase separation occurred, showed defined maxima at the locations where liquid-ordered patches appeared. For the vesicle shown in figure 3.3, after a lag-time of 20*s*, the number of patches steadily grew at a rate of $(0.116 \pm 0.005)/s$
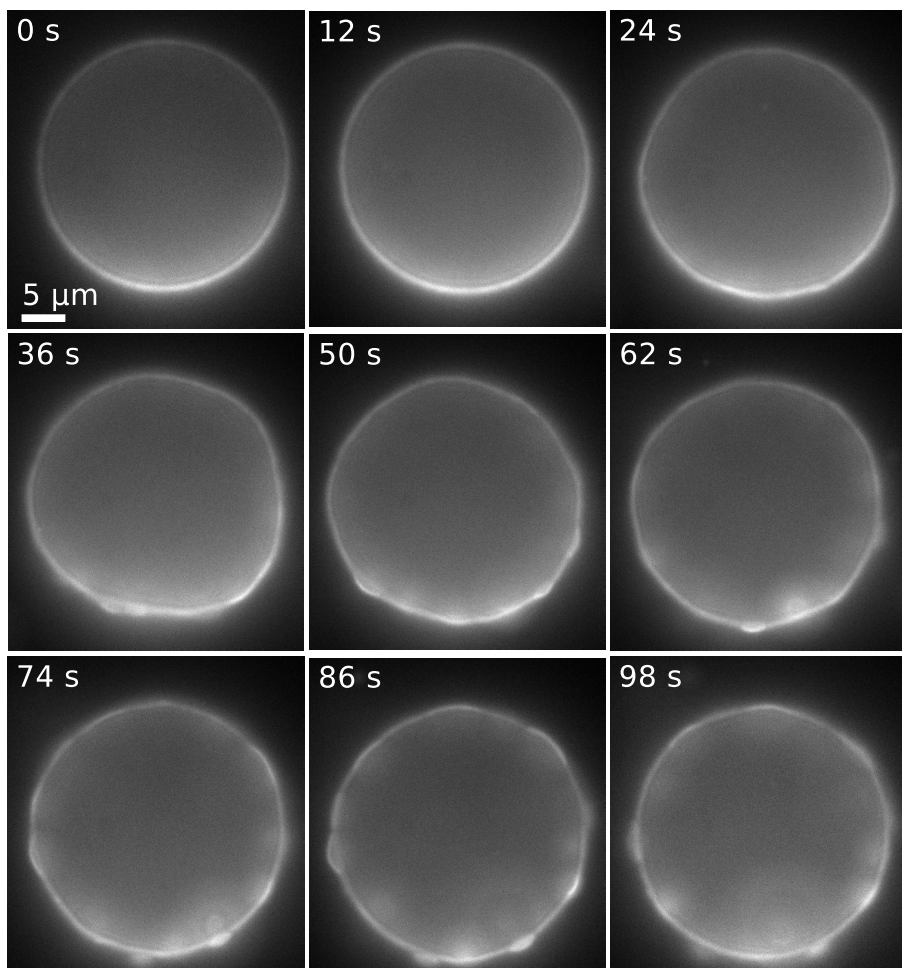
Figure 3.3: **Phase separation in a GUV followed by fluorescence microscopy.** At $t = 0\,$s, the fluorescence was homogeneouly distributed along the GUV perimeter. After a few seconds the GUV membrane started to deform. After about $20\,$s lipids started to segregate into patches. After about $40\,$s the patches formed buds.

(figure 3.4). It should be noted that the initial lag-time was not controlled, given that it was impossible to prepare all vesicles at the exact same location in the ternary phase diagram. Hence, for every vesicle, the distance to the unmixing region varied, and with that, the time at which phase separation started in our experiments. Analogous to the number of patches, the fraction of the perimeter that was covered by the liquid-disordered domain increased with time. Between 20 and 100s it increased towards 40%. In this range the conversion followed a linear relation at a constant rate of $(5.4 \pm 0.2) \cdot 10^{-3}/s$ (figure 3.5). Because only part of the time the GUV is illuminated, these numbers in terms of illumination time are $(11.6 \pm 0.5)/s$ and $(5.4 \pm 0.2) \cdot 10^{-1}/s$ respectively.
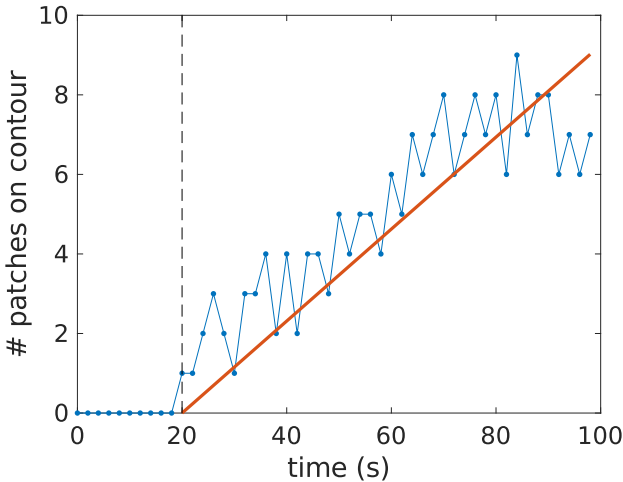
Figure 3.4: **Number of patches visible on the perimeter of a GUV.** The number grows after an initial lag-phase (black, dashed line) at constant rate of $(0.116 \pm 0.005)/s$.

The rate of lipid oxidation could be predicted, provided one knew all photophysical and photochemical rate constants [22]. Following the reaction scheme described in section 3.2.1, the rate R, at which the liquid-orderd phase will grow is expressed by:

$$R(c, I, \lambda) = c \times \alpha(\lambda) \times I(\lambda) \ \times \ \eta_{ST} \times \eta_{TT} \times \eta_{chem} \tag{3.1}$$
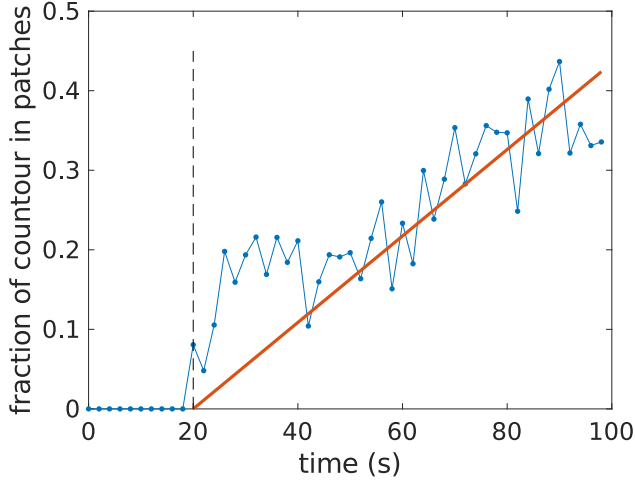
Figure 3.5: **Fraction of the contour which is in the liquid-ordered patch.** After an initial lag-phase (black, dashed line), the total area fraction grows at a constant rate of $(5.4 \pm 0.2) \cdot 10^{-3}/\text{s}$.

This rate depends on the concentration of the rhodamine dye (c), the absorption cross section of the dye at the excitation wavelength ($\alpha(561\,\text{nm}) = 2.9 \cdot 10^{-7}/\text{cm}^2$), the illumination intensity ($I(561\,\text{nm}) = 100\,\text{W}/\text{cm}^2$), the intersystem crossing yield of rhodamine ($\eta_{\text{ST}} = 1\text{–}2\%$), and the two largely unknown parameters for the triplet-triplet transfer towards oxygen (η_{TT}) and the chemical reaction efficiency of acyl-chain oxidation (η_{chem}). Yet it is obvious from equation (3.1) that $R(c, I, \lambda)$ is proportional to $c \times \alpha(\lambda) \times I(\lambda)$, which is proportional to the detected brightness in the image. Our prediction was confirmed in experiments. Various vesicle preparations were made in which the dye concentration and the illumination intensity was varied. The average brightness was compared to the rates of the fractional domain growth as displayed for one GUV in figure 3.5. The data are shown in figure 3.6 for a range in brightness between $1\text{–}9 \cdot 10^5$ counts per pixel. The behavior was linear, characterized by a slope of $(4.00 \pm 0.35) \cdot 10^{-6}$.
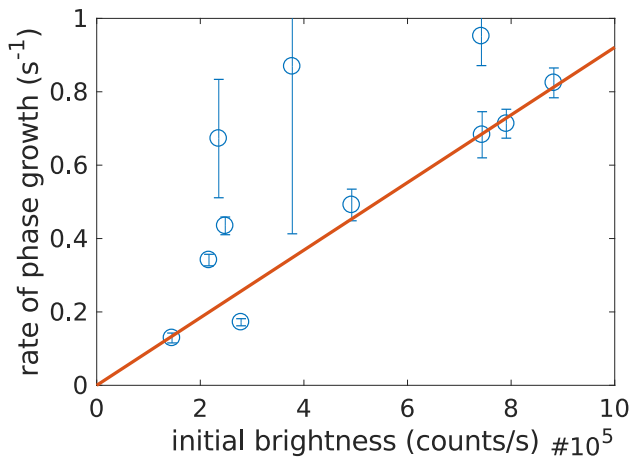
Figure 3.6: **Rate of phase growth,** expressed as a fraction of the visible contour, plotted versus the average brightness (counts/s) of the edge of the GUV in the first recorded frame. A good linear correlation through the origin exists, and the slope of the line is $(9 \pm 4) \cdot 10^{-7}$.

3.2.3 Light-induced shape fluctuations

A further, so far unnoticed observation we made in our experiments was the development of dramatic shape fluctuation that occurred before membrane domains became visible (see figure 3.3). At the beginning of the experiment ($t = 0s$) shown in figure 3.3 the GUV assumed a perfect circular shape. As the vesicle was illuminated, spatial and temporal fluctuations started to appear already after 12 s which further evolved until at 74 s a steady shape was obtained in which stable liquid-ordered domains are clearly visible that bulge out from the vesicle.

Those membrane fluctuations we in part attribute to an increase in surface area of the GUV membrane due to the different molecular shape of the converted lipids (figure 3.2). However, lipid conversion might further lead to a change in the mechanical properties of the membrane, and to a change in the spontaneous curvature [1, 2], both of which might contribute to the observed fluctuations. A general mechanical description of the mechanical properties of vesicles is obtained by the Helfrich Hamiltonian [23]:

$$H_{\text{shape}} = \int_A \, \mathrm{d}A \, \frac{\kappa_{\text{b}}}{2} \, (C_1 + C_2 - C_0)^2 \; + \; \int_A \, \mathrm{d}A \, \sigma \qquad (3.2)$$

The stored mechanical energy in the vesicle depends on its local bending rigidity, κ_{b}, its local curvatures, C_1 and C_2, on the spontaneous curvature due to the shape of the lipids C_0, and on the membrane tension σ. Additional terms in this Hamiltonian like the Gaussian curvature, an area-difference term, and the osmotic pressure were neglected in eq. 3.2 as they were constant in our experiments. At equilibrium, the vesicle will assume a shape of minimal energy [23]. Creation of excess membrane area will hence lead to a change in vesicle shape and to fluctuations around its equilibrium configuration.

3.2.4   Sub-diffraction tracking of the GUV perimeter

To quantify our observations we set out to precisely determine the position of the GUV membrane to sub-diffraction accuracy (see also section 3.4). We first determined the GUV center and its mean radius R (green circle in figure 3.7). Subsequently, closely-spaced radial sections were calculated from which the position of the membrane was extrapolated by Gaussian fitting (inset to figure 3.7). The large signal of the rhodamine-dye ($S = 1000$ counts) allowed us to determine the position of the GUV membrane to about $20 \, \text{nm}$. This precision was predicted using arguments from super-resolution microscopy [24], from which the accuracy was estimated to be $\Delta x = \Gamma_{\text{PSF}}/\sqrt{s}$ ($\Gamma_{\text{PSF}} \approx 300 \, \text{nm}$, width of the point-spread function). The red line in fig. 3.7 shows the location of the GUV membrane as determined in this way.

In figure 3.8 the deviation u of the GUV membrane from an ideal circle is shown as it varies along the perimeter. Just before phase separation occurred, these fluctuations were easily identified. u fluctuates on the length scale of $30 \, \mu\text{m}$ for up to almost one μm from the ideal circle describing the GUV. Over the time-course of the experiment, we quantified the size of these fluctuations by calculating the standard deviation of u averaged over the whole GUV perimeter. Figure 3.9 shows how $\text{STD}(u)$ changes with time between start
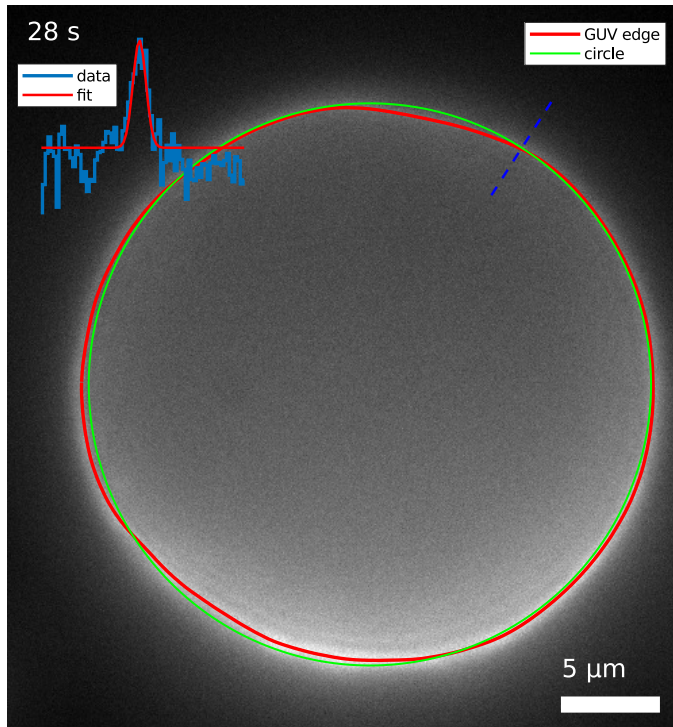
Figure 3.7: **Image of a GUV exhibiting membrane fluctuations.** The image was taken close to the time when phase separation occurred. The green circle is an ideal circle coinciding with the edge of the GUV. The red line shows the real position of the GUV membrane as determined by fitting Gaussian profiles to radial profiles. The inset in the top-left shows a Gaussian fit for one profile. Pixel values are shown in blue, the Gaussian fit is shown in red.

of the experiment and up to $100\,\mathrm{s}$ later. Before phase separation becomes visible ($t < 20\,\mathrm{s}$), $\mathrm{STD}(u) = 0.3\,\mu\mathrm{m}$, which in turn doubled to $0.6\,\mu\mathrm{m}$ at $60\,\mathrm{s}$. After phase separation was stable, the fluctuations dropped at $70\,\mathrm{s}$ to less than $0.2\,\mu\mathrm{m}$. For even longer timescales, the membrane formed buds to which our analysis did not apply, and results were not further followed.
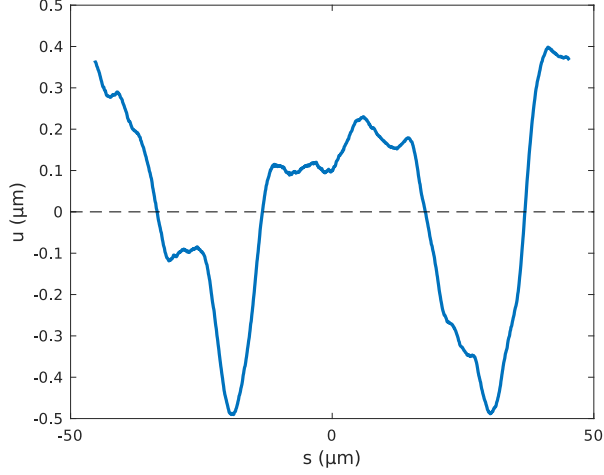
Figure 3.8: **Deviation u of the GUV membrane position from an ideal circle** at positions $s = \theta R$. In this example the difference between biggest and smallest radius is almost 1 µm.

3.2.5   Mechanical properties of the membrane througout phase separation

Fluctuations are closely related to the mechanical properties of membranes [23, 25, 26]. The mechanical properties are characterized by the bending modulus κ_{b}, and the membrane tension σ (see equation (3.2)). Both we extracted from the fluctuation spectrum [26, 27] determined from the real-space fluctuations along the vesicle perimeter (figure 3.8). The fluctuation spectral density for the data in figure 3.7 is shown in figure 3.10. Following the description developed by Pecreaux, the power spectral density is given by [26, 27]:

$$\langle |u_{\mathrm{k}}|^2 \rangle = \frac{1}{2\pi R} \; \frac{k_{\mathrm{B}} T}{\sigma q^2 + \kappa_{\mathrm{b}} q^4} \tag{3.3}$$

A fit of the spectral data to equation (3.3) is shown in figure 3.10 (red line). The fit yielded values for the bending modulus $\kappa_{\mathrm{b}} = (1.0 \pm 0.7) \cdot 10^{-19}$ J and for the membrane tension $\sigma = (2.5 \pm 0.3) \cdot 10^{-5}$ N/m^2. Both values corroborate values reported earlier [26, 27].
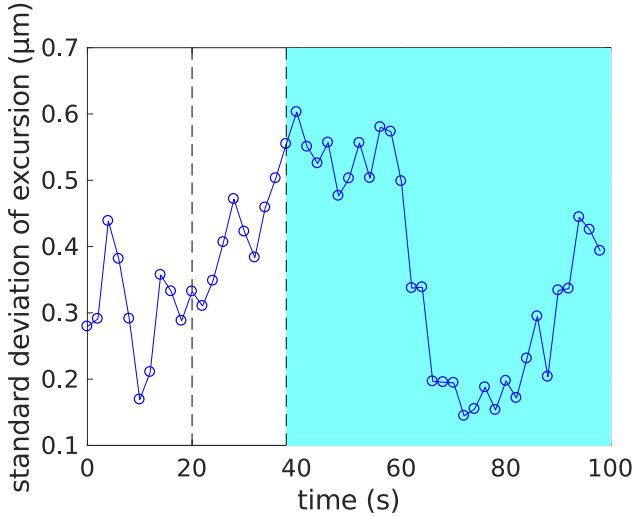
Figure 3.9: **Membrane fluctuations as a function of time.** The size of
the fluctuations we characterized for each frame by calculating the standard
deviation of u as shown in figure 3.8. The region before the first dashed line
indicates the lag-phase. The blue region after the second dashed line indicates
the time when budded patches appear in stead of pure fluctuations.

We anticipated that the bending modulus would not change when phase
separation was induced, given that the bending modulus is a material prop-
erty, depending on the composition of the membrane which only marginally
changed throughout the experiment. This hypothesis was confirmed, within
experimental uncertainty, by our experiments (figure 3.11). This finding was
further confirmed by the analysis of all GUVs. The probability density func-
tion for the bending modulus for an ensemble of all data is shown in fig-
ure 3.12. The distribution was narrowly peaked at a most probable value of
$\langle \kappa_b \rangle = (1.0 \pm 0.3) \cdot 10^{-19}$ J.

From our chemical model described earlier, which assumed that photo-
oxidation leads to a change in lipid structure and a concurrent increase in
membrane area, we predicted that surface tension, in contrast to bending
modulus, would change during the observation time. For a perfectly spherical
GUV, the volume-to-surface ratio is $R/3$. On the appearance of membrane
fluctuations, this ratio becomes smaller and consequently membrane tension
will decrease. This prediction was confirmed by our experiments (figure 3.13).
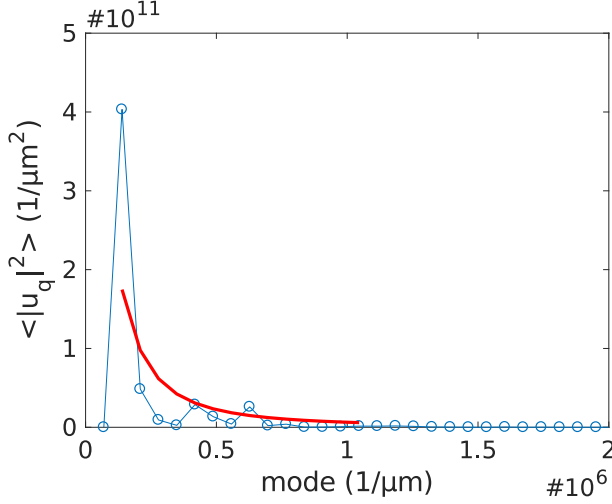
Figure 3.10: **Power spectral density of membrane fluctuations as a function of the mode** q**.** The spectrum is fitted to equation (3.3) as described in [26, 27], yielding the bending modulus $\kappa_b = (1.0 \pm 0.7) \cdot 10^{-19}$ J and membrane tension $\sigma = (2.50 \pm 0.28) \cdot 10^{-5}$ N/m^2.

Before the phase separation was visible ($t < 20$ s), σ was constant with $\sigma = \sigma_0 = (3.0 \pm 0.8) \cdot 10^{-5}$ N/m. On emergence of the phase transition the surface tension dropped to $\sigma = 1.3 \cdot 10^{-6}$ N/m. After that, phase separation was stable and clear bulged-out domains were visible ($t > 70$ s), the simple description for a vesicle as a homogeneous spherical object (equation (3.2)) clearly failed. Hence data beyond that time were further neglected. From all our measurements the distribution in initial surface tension σ_0 is shown in figure 3.14. The distribution is narrowly peaked at the most probable value of $\langle \sigma_0 \rangle = (3.3 \pm 0.3) \cdot 10^{-5}$ N/m^2.
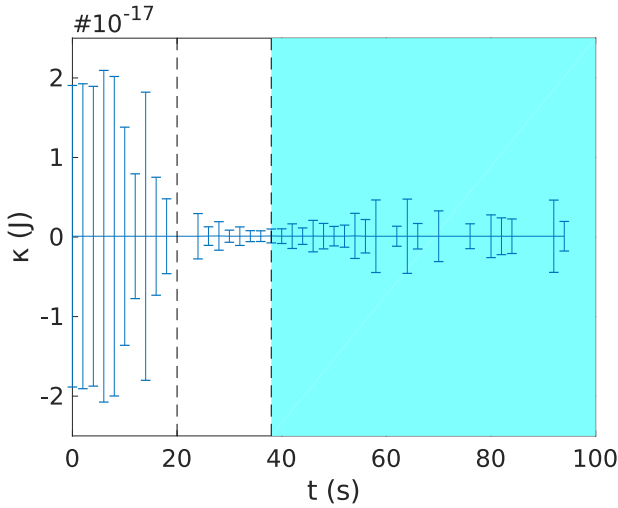
Figure 3.11: **Bending rigidity as a function of time.** During the experiment the bending rigidity did not change within experimental accuracy, and is constant around $\kappa_b = (1.1 \pm 0.1) \cdot 10^{-19}$ J.

3.3 Discussion & Conclusion

Here we investigated the physical and mechanical characteristics of phospholipid membranes when driven into a state where phase-separation occurred. Photooxidation helped us to modify the lipid composition in a gentle and controlled way. Our data on the process of photooxidation are commensurate with earlier results [1, 2, 21]: the process is based on the presence of a photosensitizer and is likely governed by the creation of a reactive oxygen species, which in turn leads to an oxidation of lipid molecules. As reported in those earlier studies, photooxidation results in an increase of surface area which has implications on vesicle stability [2] and vesicle mechanics.

While the change in lipid composition did not change the rigidity of the membrane towards bending, the membrane tension became significantly reduced. Concurrent with the reduction in membrane tension, large shape fluctuations and a separation into liquid-ordered and liquid-disordered domains occurred. We questioned whether such behavior would resemble signatures of a phase transition. With the time of experimentation, the density of high-T_m components increase, i.e. their average distance would decrease quadratically. In
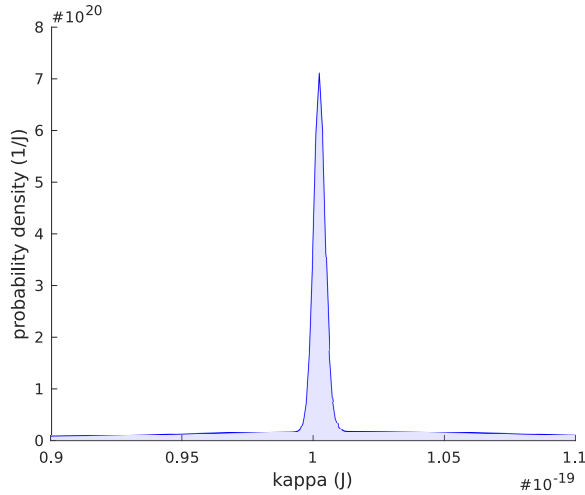
Figure 3.12: **Ensemble probability-density of membrane bending modulus.** The most probable modulus for all experiments was $\langle \kappa_b \rangle = (1.0 \pm 0.3) \cdot 10^{-19}$ J.

terms of an Ising model, this could be interpreted as a slow increase in average interaction between the high-T_m components. Concurrent with this hypothesis would be the observation of a power-law dependence of the membrane tension with time, equivalent to the interaction strength. Indeed we confirmed that hypothesis in our experiments. After the initial part in experimentation displayed in figure 3.13, the membrane tension followed a power-law dependence with an exponent of 0.99 ± 0.04. A further signature for the process being governed by a phase transition would be a universal, i.e. narrow-peaked distribution in the exponent for an ensemble of realizations. In figure 3.15, the probability density distribution of the measured exponents is shown. Although, the number of realizations was fairly small (N=9), the wide spread of the power-law dependence did not support the initial hypothesis of the observed process being covered by a phase transition of a given universality class.
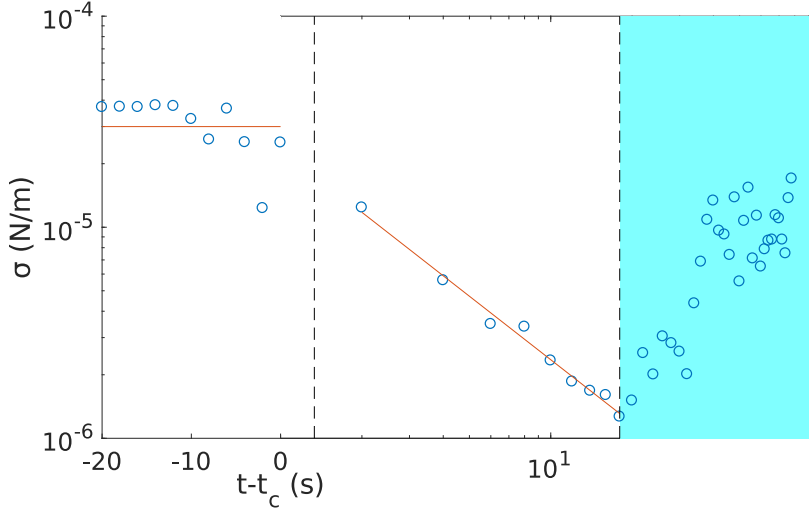
Figure 3.13: **Membrane tension σ as function of time.** An onset of fluctuations was observed at $t_c = 20\,s$ (first dashed vertical line). Before that time, the membrane tension was constant. After the onset of fluctuations, the membrane tension dropped, following a power-law behavior characterized by an exponent of -0.99 ± 0.04). When membrane patches start to evolve (second vertical line), further analysis by the simple model breaks down.

In our hypothesis, we assumed that the change in lipid composition is very slow, such that the lipid system is at equilibrium any time. In case this assumption fails, a dynamic model would apply that involves the transfer of components as well as processes for nucleation and domain growth. Which of the different models appropriately could explain our observations, hence cannot be discerned so far, and will need additional experimental evidence.

Nonetheless, we clearly demonstrated the effects of lipid oxidation on the phase behavior and the mechanical characteristics of biological membranes. Undisputedly lipid oxidation will also occur in cells, hence all the described processes will play a role. A decrease in membrane tension means that it is easier to bend the membrane. Thereby, the affinity of curvature sensing proteins can change and trigger a biological function. Cells will react on those challenges with an active exchange of lipids but also by active modulation of
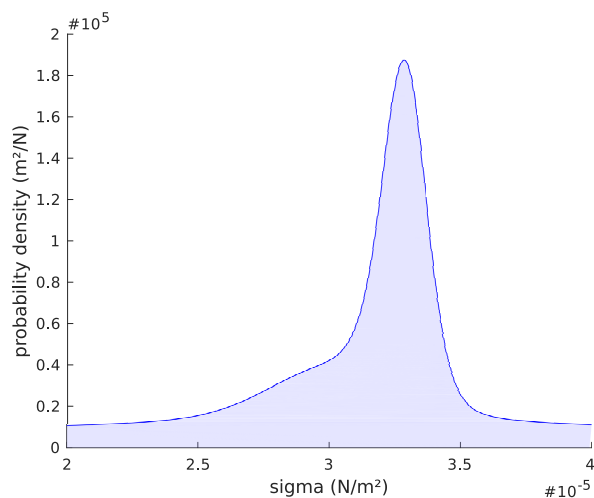
Figure 3.14: **Distribution of the initial membrane tension in all experiments.** The distribution is peaked at its most probable value of $\langle \sigma_0 \rangle = (3.3 \pm 0.3) \cdot 10^{-5}\,\mathrm{N/m^2}$.

membrane area by endo- and exocytosis. Given that those reaction mechanisms fail, cells would be driven into apoptosis, a program one tries to locally initialize in photodynamic therapy. A more dramatic effect of the enhanced membrane fluctuations would be direct cell rupture, a process which so-far has been discussed to describe the effect of photodynamic therapy, but which probably is too easy to explain the therapeutic outcome. Yet, it is interesting to note that membrane fluctuations and the parallel dramatic decrease in membrane tension might be an interesting route to follow in the current strive to built up artificial cell-like systems to mimic cell division.
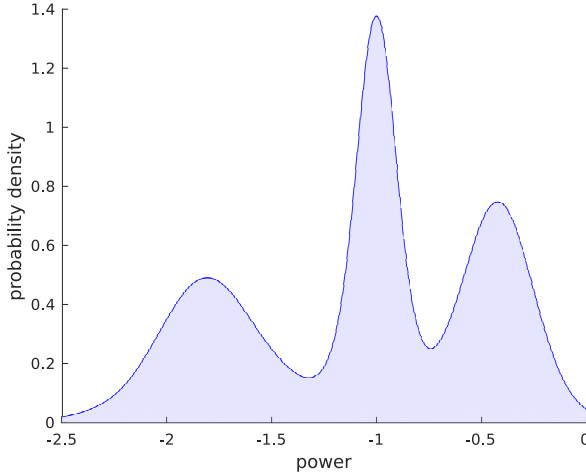
Figure 3.15: **Distribution of powers measured from the drop in membrane tension during the time of fluctuations.** While the drop shows powerlaw behavior, the powers are not unversal.

3.4 Materials and Methods

3.4.1 GUV preparation

Giant unilamellar vesicles (GUVs) were prepared using electroswelling [28]. 20 μl lipids (1-palmitoyl-2-oleoyl-*sn*-glycero-3-phosphocholine (Avanti Polar Lipids 850457C, POPC), 1,2-dioleoyl-*sn*-glycero-3-phosphoethanolamine-N-(lissamine rhodamine B sulfonyl) (Avanti Polar Lipids 810150C, DOPE-rhodamine)), sphingomyelin (Avanti Polar Lipids 860062C, Brain SM) together with cholesterol (Avanti Polar Lipids 700100P, cholesterol (plant)) dissolved in chloroform $(2\,g/L)$ were deposited on top of two indium tin oxide (ITO) coated glasses (total covered area about $10\,cm^2$). The chloroform was evaporated for two hours using a desiccator. Subsequently the coated glasses were placed parallel, coated sides facing each other in a teflon enclosure with about $3\,mm$ separation between them. The space between the glasses was filled with $230\,mOsmol/kg$ sucrose. Swelling was done for two hours at $10\,Hz$, $4\,V_{pp}$ sinusoidal excitation. After that the sucrose solution containing the GUVs was extracted from the chamber.

3.4.2   Imaging

Imaging was performed on an epi-fluorescence microscope. Illumination was performed using a 488 nm, 100 mW laser (Coherent Sapphire 488-100 CW CDRH). The laser beam was modulated by an acousto-optical tunable filter (AA-OptoElectronic, AOTFnC-VIS) to illuminate the sample only when the camera was in exposure mode. Via a tube-lens, the laser beam was coupled into a Zeiss Axiovert 100 microscope fitted with a Zeiss 100× NA 1.4 oil immersion objective resulting in Köhler illumination of the sample. The excitation and emission paths were split using a dichroic mirror (Semrock Di01-R405/488/561/635) and an emission filter (Chroma ZET405/488/561/640m). Detection was done using a CCD camera (Roper Scientific/Princeton Instruments 1340B combined with an ST133 controller and WinView32 software), cooled to −90 °C using liquid nitrogen.

3.4.3   Image Analysis

To quantify our observations we set out to precisely determine the position of the membrane of the GUV to sub-diffraction accuracy. To do this, we first determined the center position and the mean radius R of the GUV (green circle in figure 3.7). After subtraction of background by means of a spatial lowpass filter, the image of the GUV was thresholded such that pixels on the edge of the GUV were separated from the pixels outside. The locations of these pixels were subsequently used to determine the radius and center coordinates of the GUV. The GUV is then sliced into slices with an angle $\Delta\theta = 1/2R_{\mathrm{px}}$ with R_{px} the radius of the GUV measured in pixels. Now, under every radial, starting from $0.8R$ and extending to $1.25R$, one of which is shown as a blue dashed line in figure 3.7, the pixel values are fitted to a Gaussian profile. The inset in figure 3.7 shows this, with, in blue the pixel values measured, and in red the fit to them. This allows us to determine the location of the edge of the GUV with subpixel accuracy (down to about 20 nm). The red line in figure 3.7 shows the location of the edge of the GUV in the image, determined in this way. In figure 3.8 the deviation u of the edge of the GUV from the mean is shown. Just before phase separation occurs, these fluctuations can be seen visually, and the membrane can deviate up to a µm from the mean radius of the GUV. Over the course of the experiment, we quantified the size of these fluctuations by taking the standard deviation of u. Figure 3.9 shows that before phase separation happens, the GUV already exhibits fluctuations for some time. After phase separation, the fluctuations diminish and only express the height of the phase separated buds budding out from the surface.

References

[1] J. Heuvingh and S. S. Bonneau. "Asymmetric oxidation of giant vesicles triggers curvature-associated shape transition and permeabilization". In: *Biophys. J.* 97.11 (2009), pp. 2904–2912. DOI: 10.1016/j.bpj.2009.08.056.

[2] K. A. Riske et al. "Giant vesicles under oxidative stress induced by a membrane-anchored photosensitizer". In: *Biophys. J.* 97.5 (2009), pp. 1362–1370. DOI: 10.1016/j.bpj.2009.06.023.

[3] S. Reuter et al. "Oxidative stress, inflammation, and cancer: How are they linked?" In: *Free Radic. Biol. Med.* 49.11 (2010), pp. 1603–1616. DOI: 10.1016/j.freeradbiomed.2010.09.006.

[4] G. Waris and H. Ahsan. "Reactive oxygen species: role in the development of cancer and various chronic conditions". In: *J. Carcinog.* 5.14 (2006), pp. 1–8. DOI: 10.1186/1477-3163-5-14.

[5] A. Jezierska-Drutel, S. A. Rosenzweig, and C. A. Neumann. "Role of oxidative stress and the microenvironment in breast cancer development and progression". In: *Adv. Cancer Res.* Vol. 119. 2013, pp. 107–125. DOI: 10.1016/B978-0-12-407190-2.00003-4.

[6] T. D. Oberley. "Oxidative damage and cancer". In: *Am. J. Pathol.* 160.2 (2002), pp. 403–408. DOI: 10.1016/S0002-9440(10)64857-2.

[7] G. Filomeni et al. "Oxidative stress and autophagy: the clash between damage and metabolic needs". In: *Cell Death Differ.* 22.3 (2015), pp. 377–388. DOI: 10.1038/cdd.2014.150.

[8] D. E. Dolmans, D. Fukumura, and R. K. Jain. "Timeline: Photodynamic therapy for cancer". In: *Nat. Rev. Cancer* 3.5 (2003), pp. 380–387. DOI: 10.1038/nrc1071.

[9] W. Fiers et al. "More than one way to die: apoptosis, necrosis and reactive oxygen damage". In: *Oncogene* 18 (1999), pp. 7719–7730. DOI: 10.1038/sj.onc.1203249.

[10] R. C. Taylor, S. P. Cullen, and S. J. Martin. "Apoptosis: controlled demolition at the cellular level". In: *Nat. Rev. Mol. Cell Biol.* 9.3 (2008), pp. 231–241. DOI: 10.1038/nrm2312.

[11] A. Easterling et al. "A scanning electron microscopic study of the chick chorioallantoic membrane: cell death and the involvement of oxygen free radicals". In: *Scanning Microsc.* 7.1 (1993), pp. 87–96.

[12] S. J. Singer and G. L. Nicolson. "The fluid mosaic model of the structure of cell membranes". In: *Science* 175.4023 (1972), pp. 720–731. DOI: 10.1126/science.175.4023.720.

[13] D. G. Ackerman and G. W. Feigenson. "Lipid bilayers: clusters, domains and phases". In: *Essays Biochem.* 57 (2015), pp. 33–42. DOI: 10.1042/bse0570033.

[14] E. Sezgin et al. "The mystery of membrane organization: composition, regulation and roles of lipid rafts". In: *Nat. Rev. Mol. Cell Biol.* 18.6 (2017), pp. 361–374. DOI: 10.1038/nrm.2017.16.

[15] F. X. Contreras, A. M. Ernst, and F. Wieland. "Specificity of intramembrane protein – lipid Interactions". In: *Cold Spring Harb. Perspect. Biol.* 3.6 (2011), pp. 1–19. DOI: 10.1101/cshperspect.a004705.

[16] A. W. Smith. "Lipid-protein interactions in biological membranes: A dynamic perspective". In: *Biochim. Biophys. Acta - Biomembr.* 1818.2 (2012), pp. 172–177. DOI: 10.1016/j.bbamem.2011.06.015.

[17] J. Korlach et al. "Characterization of lipid bilayer phases by confocal microscopy and fluorescence correlation spectroscopy". In: *Proc. Natl. Acad. Sci.* 96.15 (1999), pp. 8461–8466. DOI: 10.1073/pnas.96.15.8461.

[18] T. Baumgart, S. T. Hess, and W. W. Webb. "Imaging coexisting fluid domains in biomembrane models coupling curvature and line tension". In: *Nature* 425.October (2003), pp. 821–824. DOI: 10.1038/nature02013.

[19] K. Simons and E. Ikonen. "Functional rafts in cell membranes". In: *Nature* 387.6633 (1997), pp. 569–72. DOI: 10.1038/42408.

[20] C. Prévost et al. "IRSp53 senses negative membrane curvature and phase separates along membrane tubules". In: *Nat. Commun.* 6 (2015), p. 8529. DOI: 10.1038/ncomms9529.

[21] C. K. Haluska et al. "Photo-activated phase separation in giant vesicles made from different lipid mixtures". In: *Biochim. Biophys. Acta - Biomembr.* 1818.3 (2012), pp. 666–672. DOI: 10.1016/j.bbamem.2011.11.025.

[22] N. Busch, M. Yarmush, and M. Toner. "A theoretical formalism for aggregation of peroxidized lipids and plasma membrane stability during photolysis". In: *Biophys. J.* 75.6 (1998), pp. 2956–2970. DOI: 10.1016/S0006-3495(98)77737-9.

[23] W. Helfrich. "Lipid bilayer spheres: Deformation and birefringence in magnetic fields". In: *Phys. Lett. A* 43.5 (1973), pp. 409–410. DOI: 10.1016/0375-9601(73)90396-4.

[24] N. Bobroff. "Position measurement with a resolution and noise-limited instrument". In: *Rev. Sci. Instrum.* 57.6 (1986), pp. 1152–1157. DOI: 10.1063/1.1138619.

[25] U. Seifert. "Configurations of fluid membranes and vesicles". In: *Adv. Phys.* 46.1 (1997), pp. 13–137. DOI: 10.1080/00018739700101488.

[26] J. Pécréaux et al. "Refined contour analysis of giant unilamellar vesicles". In: *Eur. Phys. J. E - Soft Matter* 13.3 (2004), pp. 277–290. DOI: 10.1140/epje/i2004-10001-9.

[27] S. Semrau et al. "Accurate determination of elastic parameters for multicomponent membranes". In: *Phys. Rev. Lett.* 100.8 (2008), p. 088101. DOI: 10.1103/PhysRevLett.100.088101.

[28] M. I. Angelova and D. S. Dimitrov. "Liposome electroformation". In: *Faraday Discuss. Chem. Soc.* 81 (1986), pp. 303–311. DOI: 10.1039/dc9868100303.